OPEN ACCESS

Considerations of Liquid-Phase Transmission Electron Microscopy Applied to Heterogeneous Electrocatalysis

Journal of The Electrochemical Society, 2023 **170** 056502

Considerations of Liquid-Phase Transmission Electron Microscopy Applied to Heterogeneous Electrocatalysis

Tzu-Hsien Shen,[=] Robin Girod,[=] Jan Vavra,[=] and Vasiliki Tileli[z]

Institute of Materials, École Polytechnique Fédérale de Lausanne, CH–1015 Lausanne, Switzerland

Liquid-phase transmission electron microscopy (LPTEM) is an essential tool for studying the dynamics of materials interactions at the nanoscale, in and/or with their operational environment. Microfabricated SiN_x membrane cells further allow the integration of thin-film electrodes that opens the technique to studies of heterogeneous electrocatalysts under relevant electrochemical conditions. However, experiments remain challenging and the characteristics of the dedicated electrochemical cells and of the interactions of the electron beam with the liquid electrolyte demand careful interpretation of the results. Herein, we discuss important aspects that concern the implementation of electrochemical LPTEM (ec-LPTEM). We first consider the range of information that can be accessible with the technique for electrocatalytic applications and we detail the influence of the thickness and flow of liquid electrolytes using membrane-based microcells. Further, we provide guidelines pertinent to the electrochemical configuration of the substrate working, reference, and counter electrodes. We validate these considerations by experimentally demonstrating the application of ec-LPTEM for the CO_2 reduction reaction (CO_2RR), the oxygen reduction reaction (ORR), and the oxygen evolution reaction (OER). The probed effects in metallic and oxide catalysts are directly related to the applied electrochemical stimuli and corroborate the representativity of the processes under investigation following the considerations described herein.

 [DOI: 10.1149/1945-7111/acced4]

Manuscript submitted October 5, 2022; revised manuscript received April 3, 2023. Published May 9, 2023.

Real-time monitoring of heterogeneous electrocatalytic reactions necessitates probing of complex mechano-physico-chemical interfacial phenomena.[1] Collectively, the dynamic nature of the catalyst surface and the modifications of the chemical environment around it, which take place when in contact with the fluidic electrolyte or/and upon application of potential leading to gaseous products, determine the performance in terms of activity, selectivity, and stability. Thus, extensive efforts are made to characterizing the evolution of solid-liquid-gas interfacial processes[2] under realistic operating conditions. Optical, scanning probe,[3–5] X-ray-based,[4,6–8] and electron microscopy[9] techniques have been developed for in situ and operando visualization of various electrocatalytic processes, however, they all remain difficult to implement. Their success in probing electrocatalytic processes in liquid electrolytes lies in the interplay between irradiation damage, experimental setup, phenomena that can be probed, and resolution. Within these techniques, transmission electron microscopy (TEM) has the advantage that it can be tuned to provide real-time information of morphological, structural, and chemical information down to the sub-nanometer scale depending on the choice of the recorded signals.

Electrochemical liquid-phase TEM (ec-LPTEM) became widely feasible upon the invention of the closed-cell approach. To construct the pocket of liquid for insertion in the high vacuum column of the TEMs, two microelectromechanical system (MEMS) chips are assembled with the seal formed by o-rings (Fig. 1). Different manufacturers utilize a variety of geometries for placement of the chips in the tip of the TEM holders, however, the functions of the two chips are similar in all cases. The top chip has patterned electrodes for applying appropriate electrochemical stimuli and the bottom chip is patterned with microchannels for aiding liquid wetting in the area of interest. Both chips have size-limited electron transparent areas exposing the SiN_x membranes coated on the Si substrates. Upon assembly, the electron transparent areas align, although this always takes place in a slightly different configuration each time, which can greatly affect the electrochemical performance of the system. The liquid is typically pumped using fluidic lines and streams inside the enclosure either through the holder shaft or through holes in the top chip. In both cases, the input is at a lengthy distance from the electron transparent regions to ensure stability of the liquid in the probed area. Finally, following insertion in the TEM column, the dissimilarity of the partial pressures inside and outside the cell results in outwards deflection of the thin electron transparent membranes. Overall, the miniature nature of this system augments its technical complexity and establishing methodologies for credible investigations of specific electrocatalytic reactions remains challenging.

Nonetheless, this approach has already been leveraged for probing the dynamics of electrocatalytic systems providing remarkable findings. For instance, ec-LPTEM showed catalytically relevant phase transformation of Cu nanoparticles under cathodic biasing for the CO_2 reduction reaction (CO_2RR).[10] Furthermore, dissolution/redeposition of copper nanoparticles was found to be related to size increase and morphological change of Cu nanospheres during the initial stage of CO_2RR.[11] Implementation of ec-LPTEM for oxygen reduction reaction (ORR) electrocatalysts revealed the degradation mechanisms of Pt nanocatalysts such as dissolution, detachment, nucleation and growth, migration, electrochemical Ostwald ripening, and coalescence.[12] Under oxygen evolution reaction (OER) conditions, surface amorphization of Co_3O_4 nanocatalysts during the reaction was reported to be beneficial to OER activity[13] while the surface wettability of Co-based oxide OER catalysts was reported to be influenced by electrowetting, surface redox reactions and product formation.[14] Despite the progress of the technique and scientific findings, the technically demanding system creates concerns with respect to reproducibility. To promote transparent interpretation of the results, expertise and awareness of the great number of factors at play are required.

Herein, we aim at detailing the considerations for performing ec-LPTEM experiments and interpreting their results. We first discuss the morphological, structural, and chemical information that can be accessed while operating with liquid-loaded microcells in the TEM. Second, we provide guidelines with respect to the electron-beam effects in combination with the thickness of the liquid electrolytes while demonstrating the effect of liquid flow. Additionally, we elaborate on the effects of the three-electrode system for electrocatalytic experiments and we consider the choice of working electrode material for specific reactions. Lastly, we apply the different considerations individually for following the evolution of nanocatalysts for CO_2RR and ORR and demonstrate the potential for probing in real-time the reaction product of OER catalysts using ec-LPTEM.

Electron Probing Methods

We first discuss the methods that can be utilized to probe relevant information for the study of heterogeneous electrocatalytic reactions

[=]Equal Contribution.
[z]E-mail: vasiliki.tileli@epfl.ch

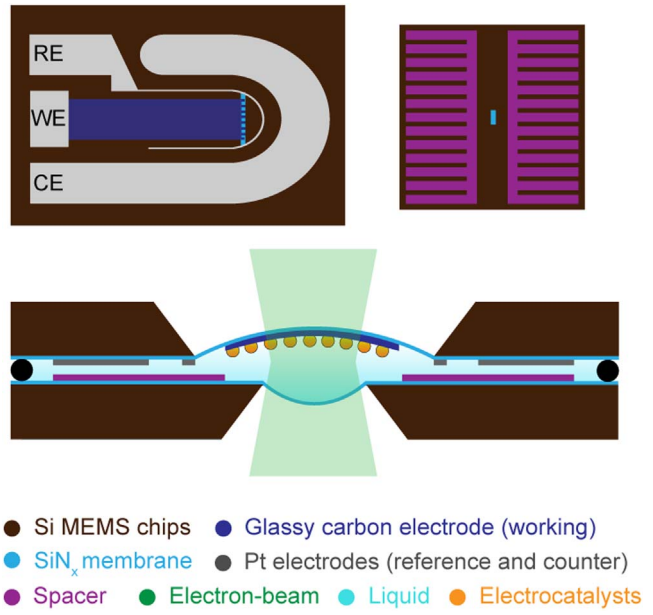

Figure 1. Schematic illustration of the internal geometry of the two MEMS chips (top-town view), showing the top electrochemical chip with the patterned working, reference, and counter electrodes (WE, RE, and CE, respectively) and the spacer chip. Upon assembly, they form the liquid-cell electrochemical enclosure (shown in cross-section).

in LPTEM. We focus on transmission mode for imaging and diffraction analyses and discuss chemical information under the requirement of operating in scanning transmission mode for site-specific information. We note that electron imaging in convergent beam illumination conditions is omitted due to the fundamental differences in signal acquisition for image formation with parallel beam illumination operation that ultimately lead to low temporal resolution in scanning TEM (STEM). Methods to improve the STEM imaging conditions in liquid microcells are ongoing.[15]

Morphological information.—The quality of TEM imaging in liquids is directly linked to the thickness of the liquid layer and the overall thickness of the cell when inserted into the microscope column. The in-plane liquid-cell path that the electrons need to transmit through results in strong inelastic scattering, which effectively reduces the spatial resolution.[16] To minimize this effect, zero-loss energy-filtered TEM (EFTEM) that filters the inelastically scattered electrons and improves image quality is applied. The enhancement in quality is illustrated in Fig. 2a. Bright-field TEM (BFTEM) images of a Pt substrate wetted with an alkaline solution were acquired without and with the zero-loss energy filtering mode. The BFTEM images were acquired in a JEOL2200FS TEM at 200 kV equipped with an in-column omega filter. Zero-loss EFTEM images were taken by placing an energy slit with the width of 12 eV at the zero-loss peak. The EFTEM imaging of the particles and liquid was performed in a liquid electrochemistry TEM holder (Hummingbird Scientific). The liquid cell was assembled using customized MEMS chips (made in EPFL's CMi cleanroom) and a spacer chip (1 μm, Hummingbird Scientific). The customized MEMS chip was patterned with three Pt thin-film electrodes (15 nm with 5 nm Ti adhesion layer underneath), and the SiN_x membrane thickness was 41 nm measured by a spectroscopic reflectometer.

The polycrystalline structure of the Pt substrate appears clearer and less blurry with zero-loss filtering, as demonstrated in Fig. 2a. To quantitatively evaluate the differences, the fast Fourier transform (FFT) patterns of the TEM images were analyzed with respect to the circularity of the diffused rings and the eccentricity metric was calculated. The FFTs of the TEM images were calculated in GMS software (Gatan). Gaussian blur filtering was applied on the FFT

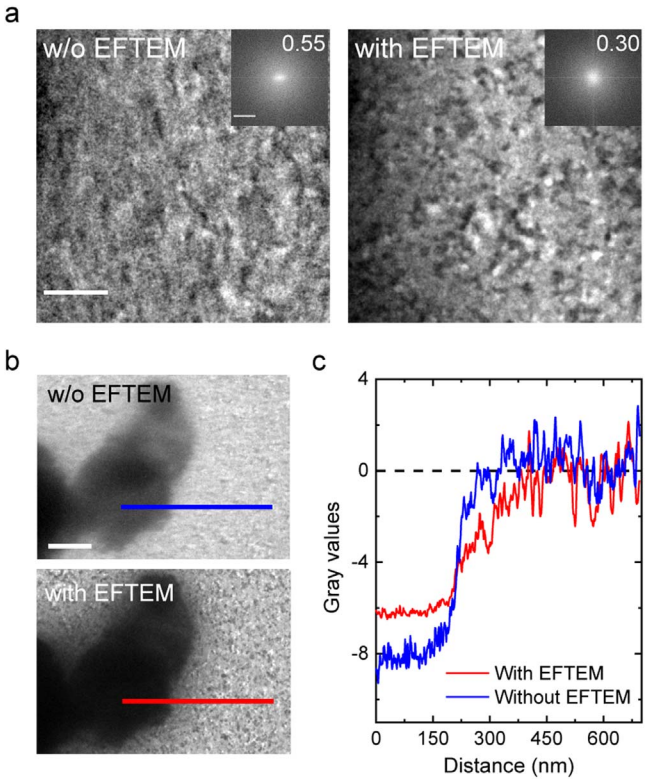

Figure 2. Comparison of BFTEM images without and with zero-loss energy filtering. (a) BFTEM images of the Pt thin-film electrode enclosed in SiN_x membrane liquid cell without and with EFTEM. Scale bar is 100 nm. The inset images show the corresponding FFT patterns of the TEM images. Scale bar is 0.2 nm^{-1}. The values on the top-right insets indicate the eccentricity metric. (b) BFTEM images of catalytic particles on Pt substrate in a liquid-cell enclosure. (c) Line profile of the gray values across the particles. The gray values of the images were normalized to the region of the Pt substrate. Scale bar is 200 nm. Red and blue lines are with and without EFTEM, respectively.

patterns with a sigma value of 10 in Fiji software. Renyi's entropy thresholding method was applied to segment the low spatial frequency in FFT patterns (with the values 182 to 255). The segmented patterns were then fitted with an oval shape to calculate the major a and minor b axes. The eccentricity was calculated by taking the square root of $1\text{-}b^2/a^2$. The larger eccentricity value of the unfiltered BFTEM image with respect to the filtered one (0.55 vs 0.30) indicates its distortion, as a result of including the inelastically scattered electrons in the image formation. Upon deposition of catalytic particles, the beneficial effect of utilizing zero-loss energy filtering becomes more obvious. Figure 2b shows unfiltered and filtered BFTEM images of an oxygen-evolving oxide catalyst that sits on a Pt thin-film electrode wetted by an aqueous electrolyte. The line profile across the edge of the particle in Fig. 2c shows that the change of the contrast in the EFTEM image is less abrupt at the interface. In fact, the liquid layer surrounding the particle becomes visible once the inelastically scattered electrons traversing the liquid are removed by application of zero-loss energy filtering. Thus, zero-loss EFTEM imaging can also provide the capability to probe the liquid surrounding catalytic particles.

We note that the absolute thickness of the liquid inside the microcell is critical for enhancement of image quality with EFTEM. Typically, a relative thickness in units of t (thickness in the direction parallel to electron beam) over λ (inelastic electron mean free path) in the range of 2 is advised. More details on the cell's liquid thickness are given later.

Structural information.—Similar to TEM imaging, energy filtering can improve selected area electron diffraction (SAED)

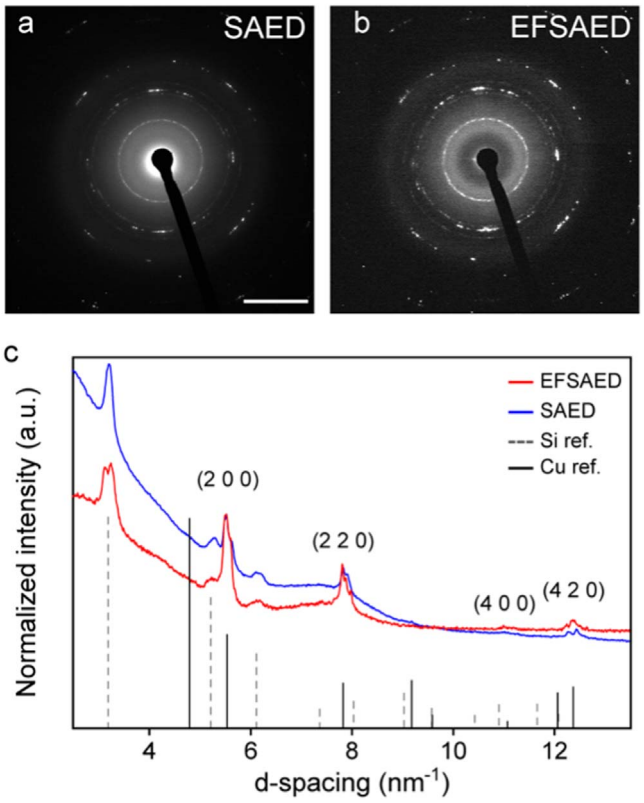

Figure 3. Comparison of ufiltered (a) and energy filtered (b) SAED patterns of Cu nanoparticles in thin liquid layer. Scale bar is 5 nm^{-1} (c) Rotational average of the SAED patterns with reference data of Si and Cu reflections (gray-dashed and black-solid linnes, respectively). Total intensity was normalized to the intensity of Cu (200) reflection.

patterns for obtaining high-quality structural data of catalysts in liquids. This effect is demonstrated in the SAED of Cu nanoparticles dropcasted to a sub-monolayer coverage on an electrochemical chip featuring a 50 nm SiN_x membrane and a 20 nm thin-film glassy carbon substrate wetted with a 0.1 M $KHCO_3$ aqueous electrolyte. Images of the particles on the chips are available in Ref. 11. The two diffraction patterns were collected in a short sequence, where the total liquid thickness was assumed to be constant, based on the mass-thickness contrast pre- and post-acquisition. The effect of energy filtering on the SAED pattern was consistent when the filtered and unfiltered patterns were acquired continuously in an alternating sequence, further ascribing the observed effects to energy filtering, as opposed to varying liquid thickness.

The inelastically scattered electrons contribute to a strong and diffuse background that makes the kinematical reflections less visible in the unfiltered diffraction pattern (Fig. 3a). By applying zero-loss energy filtering, the inelastic background (a collective result of the membranes, liquids, electrodes, and catalyst materials) can be effectively eliminated (Fig. 3b). To quantitatively compare the signal-to-background ratio in the SAED patterns, the rotational average of the intensity in the patterns was calculated, and the intensity was normalised to the peak that is assigned to Cu (200) reflections. The diffraction peaks match the Cu reflections viewed from [001] zone axis. We note that the Si reflections found in the SAED patterns stem from the Si adhesion layer underneath the glassy carbon. Overall, as shown in Fig. 3c, the improved signal-to-background ratio is apparent in the filtered SAED compared to the unfiltered pattern and the improvement of diffraction analysis in energy-filtering mode for ec-LPTEM measurements becomes apparennt.

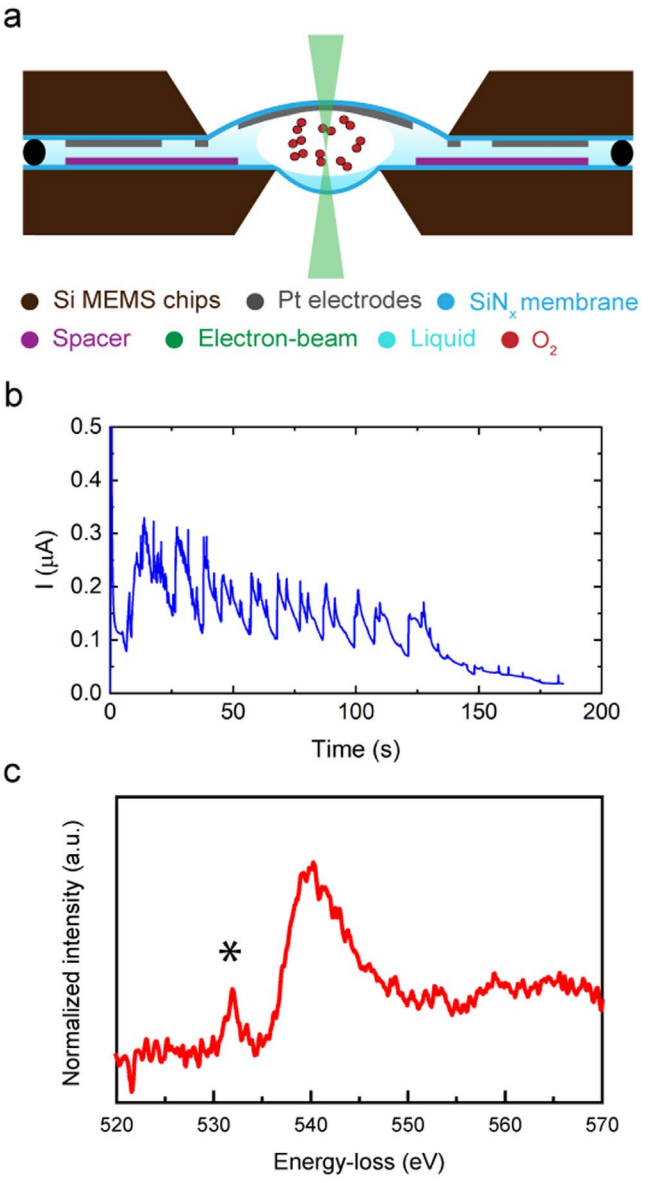

Figure 4. Probing the electrolytic molecular oxygen formation in liquid phase STEM with EELS. (a) A schematic illustration of an O_2 bubble in a liquid-cell enclosure upon application of a high anodic potential. (b) Chronoamperometry profile at the applied potential of 2.5 V vs RHE. (c) EEL spectrum of the O K-edge. The peak at 531 eV indicates the presence of molecular oxygen.

Chemical information.—Acquisition of real-time chemical information of electrocatalytic processes is more challenging than imaging and diffraction analyses. The main difficulty has to do with the requirement of considerable electron-beam exposure times for detection of the analytical signals. For energy dispersive spectroscopy (EDS), which is commonly performed for elemental analyses, the X-ray signal collected by the detectors is inhibited by the configuration of TEM liquid cells based on MEMS chips. Liquids, silicon nitride membranes, and electrodes reduce the intensity of the emitted X-ray signal arriving to the EDS detectors. Moreover, the location of the EDS detectors (above the sample) induces instrumental limitations for EDS signal collection, which are not compatible with the current liquid-cell designs. For example, Si substrates at the backside of the MEMS chips and the clamps on the holder tip limit the solid angle for the emitted X-ray signals,

reducing the EDS collection efficiency. The alternative analytical method in TEM, electron energy-loss spectroscopy (EELS), is considered to be more suitable for real-time chemical probing of electrocatalytic processes in liquids. In contrast to EDS, EELS detectors are located under the sample, collecting the signals in transmission mode, which provides better acquisition efficiency in liquid-cell samples. Valence (EELS) probing in liquid-cell enclosures was previously demonstrated for probing the deposited metallic copper particles induced by electron-beam radiation.[17] Recently, core-loss EELS was used to acquire information about the reaction products in liquids,[14] establishing its potential for probing chemical changes in real-time in the liquid cell.

Figure 4 depicts the capability of EELS for detecting gaseous electrocatalytic products. The cell was initially filled with 0.1 M KOH electrolyte and then a high anodic potential at 2.5 V vs. reversible hydrogen electrode (RHE) was applied to generate molecular oxygen from the ultra-thin Pt electrode. The O_2 formed a gas bubble as shown in Fig. 4a. The oxygen K-edge EEL spectra were acquired in STEM mode using Gatan GIF Quantum ERS in a Thermal Fisher Scientific Themis STEM at 300 kV. The convergent and collection angles were 8 and 19.8 mrad, respectively. The probe current was 0.3 nA, the entrance aperture was 2.5 mm, and 0.1 eV ch^{-1} dispersion was used for the EELS acquisition. DualEELS acquisition with high-loss time of 0.1 s and low-loss time of 0.0001 s was applied. Spectrum Imaging was acquired with pixel dwell time of 0.2 s. The spectrum was summed over 400 pixels. The experiments were performed using a liquid electrochemistry TEM holder (Hummingbird Scientific). The liquid cell was assembled using customized MEMS chips (made in EPFL's CMi cleanroom) and a spacer chip (100 nm, Hummingbird Scientific). The customized MEMS chip was patterned with three Pt thin-film electrodes (15 nm with 5 nm Ti adhesion layer underneath), and the SiN_x membrane thickness was 41 nm, measured by a spectroscopic reflectometer. The EEL spectra were acquired during chronoamperometry (Fig. 4b).

Figure 4c shows the O K-edge after the formation of molecular oxygen bubble. The peak feature at 531 eV is attributed to the energy-loss of the transmitted electrons due to the transition of inner shell electrons to anti-bonding states in the molecular oxygen (1 s→π^*), indicating the presence of molecular oxygen. The signal of the broad peak at ∼540 eV in the spectrum is attributed to the oxygen in the silicon nitride membranes and liquid electrolyte. This example demonstrates the potential of EELS for acquiring site-specific analytic information of electrolytic processes in situ in the TEM under optimized cells and electron-beam conditions.

Considerations of Electron Imaging in Liquids

Next, we consider the operation of the liquid cell in the TEM and the implications of imaging with electrons through a thin layer of liquid electrolyte. We discuss the interactions of the electron beam with the electrolyte and the importance of the liquid thickness on the resolution, and we present a method for probing the flow of electrolyte through the observation region.

Electron-beam induced effects.—A critical effect of the impact of the electron beam in liquids is radiolysis. For water-based liquid solutions, it is reported that radiolysis can lead to the production of a series of species ($H_2O \rightarrow H^+$, OH^-, e^-_{aq}, $H^\cdot$, $OH^\cdot$, H_2O_2, H_2,etc) that are highly influenced by the electron dose rate.[18] Importantly, some of the free radicals in radiolytic species can be strongly oxidizing or reducing and can react with other radiolysis products in the solution, which can be particularly detrimental for probing electrocatalytic processes. Simulations of the electron-beam induced effects on the concentration of radiolysis species in aqueous solutions have shown that the chemical changes also depend on the initial composition of the solution.[18] For example, radiolysis can generate H^+ ions, which makes aqueous solutions more acidic, reducing the pH values of the electrolytes. Alkaline solutions are more affected by radiolysis than acidic electrolytes. It has been reported that the pH value of alkaline solutions can be reduced to ∼8 at a high electron dose rate.[18] Reducing the electron dose can mitigate some of the effects of radiolytic products but it can also have a negative impact on image quality and resolution.[16] Recent advancements in direct electron detection systems provide a new opportunity for realizing minimum electron dose in liquid-cell TEM with the added advantage of providing higher temporal resolution, which is beneficial for capturing the evolution of transient states or early stages of catalytic reactions.[11] Apart from reducing the electron dose rate, it has been shown that adding scavengers such as ethanol and isopropanol in the electrolyte can mitigate the production of undesirable radiolysis damage of materials inspected in liquids.[19,20]

The effects due to the electron beam render control experiments imperative. These should in the first place determine the electron dose rate limit at which no direct observable damage is visible. However, even if direct electron-beam induced damage is limited, the modifications imparted to the environment may modify and/or accelerate the degradation of catalysts upon electrochemical stimulus.[12,21] Therefore, further controls to understand the extent of these modifications are typically necessary and may include pre-studies with identical-location examinations and controls after in situ electrochemical experiments of nanoparticles deposited on the electrode but outside of the e-beam illuminated area.

Liquid thickness.—The liquid thickness is one of the most critical parameters that influence the (S)TEM analyses. As the liquid cell is inserted in the column of the microscope, it is subjected to the pressure difference between high vacuum (outside) and almost ambient pressure (inside the cell). Thus, the low-stress, thin SiN_x membranes that seal the liquid may bulge under this pressure difference.[22] If the liquid completely fills the cell, the actual liquid thickness due to bulging of the membranes is thicker than the gap defined by the spacer and may range up to several micrometers. The liquid thickness can be reduced by forming a thin wetting liquid layer with gas or vapor present within the rest of the enclosed cell.[23–25] When the liquid forms a thin wetting layer on the interior surfaces of the liquid cell, the imaging resolution and contrast is improved remarkably. Sub-nanometer resolution TEM imaging of Pd nanoparticles confined in such a thin-liquid layer was reported when a gas bubble was generated by e-beam radiolysis.[24] Additionally, it was shown that gas can be generated by electrolyzing the aqueous solution with application of external electric potential to achieve thin wetted liquid conditions.[12,25] However, a thin liquid layer configuration can also result in higher solution resistance, which gives rise to larger ohmic drop in the electrochemical measurements.[26] Furthermore, the reduced geometrical cross-section of the thin liquid layers can also lead to diffusion and mass-transport limitations and depart from the bulk electrolyte behavior. This effect can be particularly pronounced in cases where the electrochemical response is primarily determined by mass-transport, i.e., with fast kinetics.[27] However, electrocatalytic systems are more typically limited by the kinetics or charge transfer rate at the catalyst/electrolyte interfaces and may be less influenced by the amount of the liquid electrolyte. Finally, we note that full control over the liquid thickness is challenging during electrocatalytic experiments where electrowetting, electric field, and/or electric current distributions can cause movement of the liquid during the processes.

Measurement of the liquid thickness in the liquid cell is a complex issue for ec-LPTEM.[28] When the liquid fully fills the cell, the liquid thickness is defined by the distance parallel to the electron-beam direction between the two SiN_x membranes. As the SiN_x membranes bulge under the pressure difference, the gap between them defines the liquid thickness. The gap typically includes the height of the spacer and the displacement due to bulging of the membrane windows, which depends on the mechanical properties of the SiN_x membranes.[22] In these full liquid immersion conditions, a more empirical way to estimate the liquid thickness inside the cell is

to measure the relative thickness which is defined as t over λ using EELS. The relative thickness is determined by the ratio of the number of zero-loss electrons (I_0) to the total number of incident electrons (I_t) in EEL spectra, following Beer–Lambert's law, $t/\lambda = -\ln(I_0/I_t)$. The overall relative thickness includes two contributions: the relative thickness of the dry cell and the liquid. By subtracting the relative thickness of the dry cell, the actual liquid thickness t_{liquid} can be expressed by:

$$t_{liquid} = \left[\left(\frac{t}{\lambda}\right)_{overall} - \left(\frac{t}{\lambda}\right)_{dry\ cell}\right]\lambda_{liquid}.$$

The relative thickness of the dry cell can be measured by EELS of an empty cell under the same acquisition conditions while the λ_{liquid} depends on the examined liquid. For instance, the thickness of thin films of liquid water has been estimated experimentally by establishing the well-defined liquid thickness.[29] However, when a thin liquid layer wets the electrochemical chip, the cell can also contain gaseous/vapor components. In this case, t/λ provides an overall thickness of the cell and the relative contribution of the liquid with respect to the vapor is challenging to estimate.

Liquid flow.—Another important aspect of LPTEM experiments is the control over the liquid flow through the imaging region. This aspect is intimately connected to the design and geometry of each liquid-cell setup. The earliest designs featured on-chip liquid reservoirs and relied on gluing the assembly together[30] whereas modern commercially available liquid-cell holders are an open system with a liquid inlet and outlet, connected via tubing to the exterior of the microscope, that rely on compressible o-rings to make the vacuum seal between the interior and exterior of the holder. Furthermore, there are channels engineered into the tip to direct the liquid flow into the imaging region between the two window chips, with the technical solution of this differing between manufacturers. While Hummingbird Scientific holders allow for liquid bypass around the spacer chip, the other two design force the flow between the two chips, either with the use of gaskets (Protochips) or with liquid vias going through the chip (DENSsolutions). In all cases, the liquid flow is never directed exclusively through the imaging area.

To understand the liquid flow characteristics regardless of the liquid-cell holder, a method for its visualization is presented. Fluorescent tracking particles (TP) were dispersed in the liquid phase and a flow rate through the tip was controlled with a syringe pump. The TPs were imaged with a widefield epifluorescence microscope (Zeiss LSM 700), where a monochromatic light source excited the fluorescence emission of the particles specifically. The technique is well suited as it allows to keep the entire z-height of the liquid in focus and provides fast acquisition where the fluorescent contrast of individual nanoparticles can be reliably captured. The videos were then analyzed with iterative particle imaging velocimetry (PIV) method available either as an ImageJ plugin[31] or a standalone open-source software.[32] In principle any contrasting particles that form a stable dispersion in the liquid under investigation can be used to visualize the flow. Here, we employed 280 nm silica TPs doped with fluorescein, synthesized according to previously published protocols[33] or commercially available 250 nm polystyrene TPs doped again with fluorescein (micromer-greenF, Micromod). We found these well-suited for flow visualization in assembled cells with spacer thickness of 500nm and above.

The resulting flow velocity is reported in Fig. 5. Positions of the chip window transparent area and spacer window transparent areas are outlined (Fig. 5a). For this experiment, we monitor the area, where the spacer window enters the field of view (FOV). In the vector flow field, the individual vectors represent local liquid velocity over the imaged area (Fig. 5b). A mean channel flow speed as a function of the external flow rate is plotted for experiments with spacer thickness of 0.5, 1, and2 μm (Fig. 5c). Note that the vector quantity is referred to as a flow velocity, where the magnitude of the vector as a scalar value is referred to as flow speed. The flow speed maps at specified external flow rates are then plotted in Fig. 5d.

In all investigated regimes we observe laminar flow, which is typical for microchannels. The small characteristic linear dimension results in a low Reynolds number.[34] In the presented data, the liquid enters the field of view on the right side, with higher velocity in the

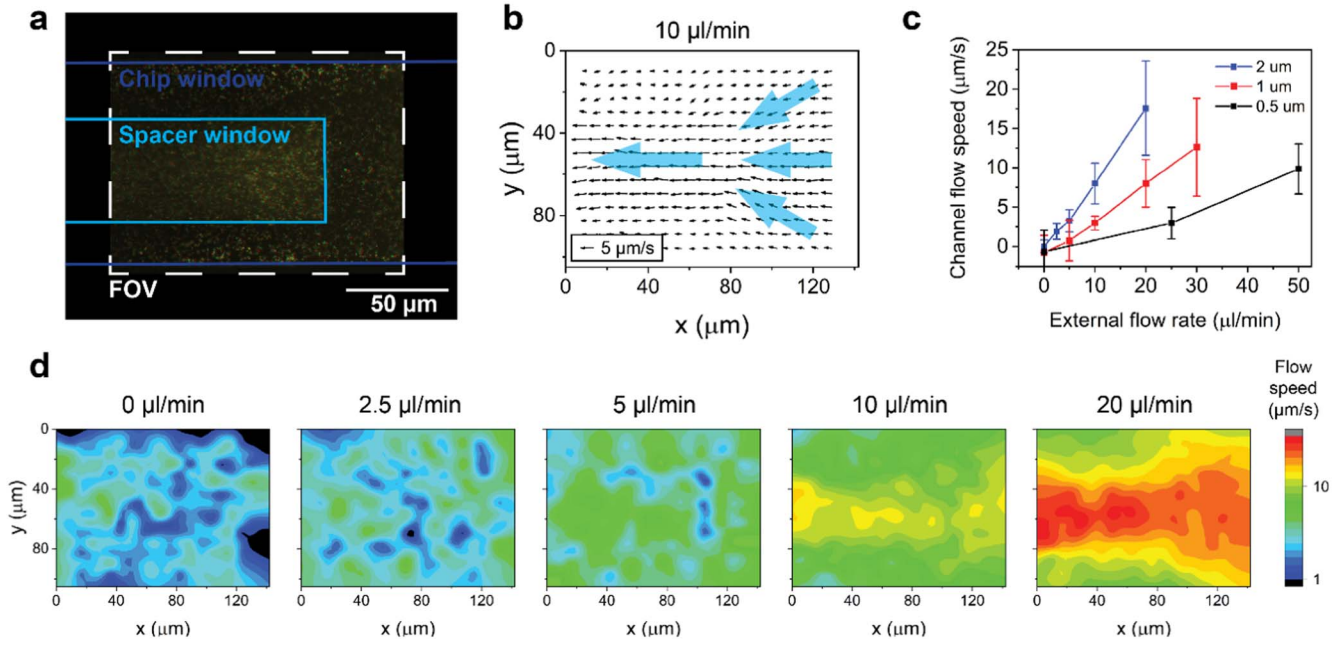

Figure 5. Method of flow visualization in a LPTEM microcell using aqueous dispersion of 280 nm silica particles doped with fluorescein for flow tracking. (a) Overlay of two subsequent frames from an epifluorescence microscope capture. Particles move in 75 ms from frame 1 (green channel) to frame 2 (red channel). Chip and spacer window position is overlaid with the field of view (FOV). (b) Result of PIV analysis showing the map of velocity vectors for 10 μl/min external flow rate and 2 μm spacer chip thickness. Blue arrows summarize the trends in velocity direction. (c) Mean channel flow speed as a function of the external flow rate for spacer thickness of 0.5, 1, and 2 μm. Error bars represent standard deviation. (d) Flow speed maps for set external flow rates between 0 to 20 μl/min (panel caption). Spacer thickness of 2 μm was used, unless specified otherwise.

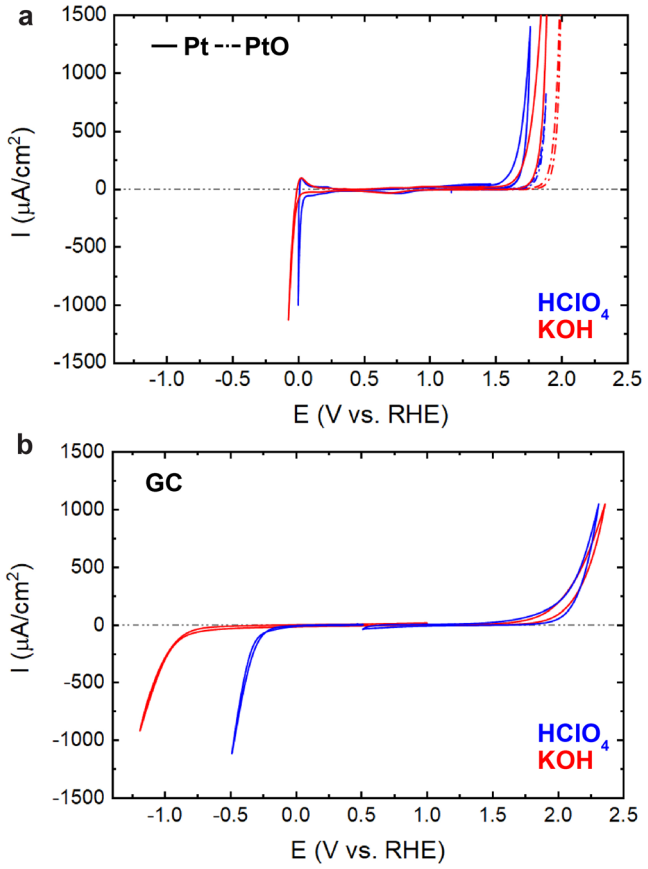

Figure 6. Cyclic voltammetry of (a) glassy carbon and (b) platinum thin-film electrodes patterned on a chip for ec-LPTEM, in 0.1 M KOH and 0.1 M $HClO_4$. Scan rate was 20 mV/s. In the case of Pt, the activity towards OER was evaluated for an electrode passivated by an oxide film after an air-plasma treatment (dotted line, 30 s, 100 W) and for the same Pt electrode after electrochemical reduction of the oxide film (plain line). The chips were fabricated in-house and the voltammograms were recorded in a benchtop, ex situ, apparatus with a true reference electrode (Ag/AgCl for $HClO_4$ electrolytes or Hg/HgO for KOH electrolytes).

middle of the channel (Fig. 5b) where we expect the highest liquid thickness due to the membrane deflection. As the liquid approaches the spacer window, it is directed towards it, where the y-component of the velocity is the highest. The liquid further accelerates in this flow channel, where the total thickness is the largest. This channeling behavior is more pronounced at higher external flow rates, where the membrane deflection is higher. This phenomenon is consistent for all investigated spacer thicknesses (data not shown) and results in increased flow speed standard deviation at higher flow rates (Fig. 5c). Overall, we found a linear dependence between the external flow rate and channel flow velocity, where thicker spacers favor the flow through the imaging region over the liquid bypass at any given external flow rate. Interestingly, there is a flow onset, i.e., a minimal external flow rate that induces flow between the chips. The first non-zero flow velocity datum for each spacer thickness in Fig. 5c corresponds to this flow onset.

It is well-documented that the thin SiN_x membranes deflect due to the pressure difference between cell inside and the vacuum of the microscope.[35] The presented flow fields were captured with the cell at atmospheric pressure, therefore the membrane bulging is induced only by the liquid flow. We measured the pressures on the syringe side of the system and found the pressures to be up to 4 bar for the higher flow rates. It is therefore expected that the observed high flow rate/high pressure channeling profile observed here is developed from the flow onset when the liquid cell is placed in the vacuum of the microscope. The presented flow experiments demonstrate that sufficient external flow rate does induce flow in the imaging region, which is beneficial to extract products and supply reactants into the small reaction volume in the ec-LPTEM system. In principle, an identical image processing workflow as presented here can also be used to directly analyze flow fields in cells inside a TEM with the use of suitable high-contrast nanoparticles.

Considerations for Electrocatalytic Measurements in Microcells

In the ec-LPTEM apparatus, electrochemical stimulus is provided through a dedicated electrochemical chip onto which co-planar thin-film electrodes are patterned by microfabrication techniques. Conventionally, three electrodes are featured and used as working, reference, and counter electrodes (WE, RE, and CE, respectively) and, in this section, we discuss the attributes of each with details on design and material choice for common electrochemical processes.

Working electrode.—The substrate used at the WE supports the catalysts and is therefore subject to the same electrochemical conditions. Key attributes that are shared with bulk cell design should be (electro)chemical stability, good conductivity, mechanical stability, and, ideally, absence of interfering electrochemical processes, to allow for straightforward identification and analysis of electrochemical features of the loaded catalytic material.[36] Additional considerations that need to be made in the context of ec-LPTEM include the possibility to pattern the material at nanoscale with established microfabrication techniques and the optimization of imaging contrast that is influenced by the crystallinity and atomic weight of the element(s). Finally, it is often beneficial to use a dielectric material with good adhesion properties as passivation layer to cover the peripheries of the cell. Typically, SiO_2 or SiN_x insulating layers are used to restrict electrochemical events to the observable area, but also to reduce the background signal from the substrate arising from capacitive current, change of phase, or other background electrocatalytic processes. Regarding the shape of the electrode, considerations should be given to the observable area, for instance maximizing the length of the electrode edge, which provides suitable imaging conditions in the case of a non-electron transparent substrate. It is also useful to keep part of the observed area free of conductive material, which provides a control to compare catalysts that are not influenced by the primary electrochemical process during the experiment.

Typical substrate materials include gold, platinum, and glassy carbon. Gold and platinum offer the advantages of metallic substrates that have to do with good conductivity, low charge transfer resistance, as well as batch-to-batch reproducibility owing to well-established microfabrication procedures for these metals. In addition, they can be plasma-cleaned to tune the surface hydrophilicity without damage and they offer good adhesion to passivation materials. Gold however tends to exhibit island growth,[37] requiring a minimum thickness of around a few tens of nm while platinum can more easily be fabricated down to a thickness of ∼15 nm while maintaining continuity. They both exhibit electrochemical features related to their surface oxidation, which limit their inert potential range in the anodic region to about 0.8 V vs. RHE for Pt and 1.3 V vs. RHE for Au.[36,38–41] While such features do not prevent the use of these substrates at more anodic potentials, care should be taken to separate the electrocatalytic processes. It is recommended to become accustomed to the substrate signals by running blank experiments to measure substrate current and identify background features prior to in situ experiments. Furthermore, repeated cycling above the oxidation potential in longer experiments can result in significant dissolution of the substrate.[42] The dissolved species can then be redeposited in the area of observation by electron-beam induced reduction,[18] or electrodeposition when the potential is cycled down to sufficiently cathodic values.[18] Ultimately the evolution of oxygen and hydrogen at these surfaces limits the usable potential range in the anodic and cathodic region respectively as gas evolution disrupts the imaging conditions. Gold is poorly active towards HER,[43,44]

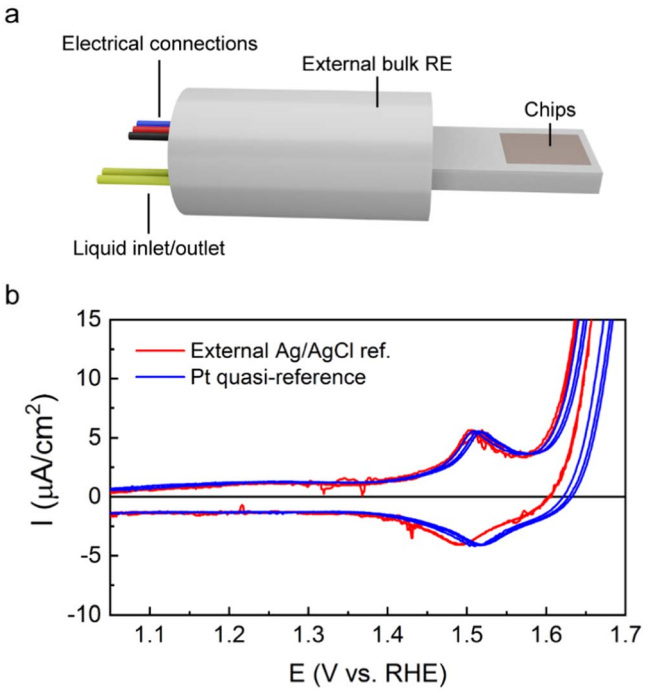

Figure 7. Calibration of Pt quasireference using an on-a-tip bulk reference electrode. (a) Schematic illustration of bulk reference electrode on the tip. (b) Representative CVs of Co_3O_4 using external bulk Ag/AgCl (red line) and Pt quasireference electrode (blue line).

making it a potential candidate for the study of catalysts at mild cathodic potentials.[43] On the other hand, platinum is one of the most active materials towards HER[43,44] but shows comparatively poor activity towards OER.[45] It is also known that OER activity at platinum surfaces exhibits a dependency on the thickness of its surface oxide film.[46,47] In practice, we have found this to be the case after air-plasma treatment, such as commonly done to improve hydrophilicity and allow for wetting of the microcell. Typically, the increased oxide layer allows Pt electrodes to be used for in situ experiments in alkaline conditions at up to 2.0 V vs. RHE. To demonstrate this, Fig. 6a compares the cyclic voltammetry (CV) results of a Pt thin-film electrode with and without an oxide film in 0.1 M $HClO_4$ and 0.1 M KOH. The oxide film was formed after a 30 s exposure to a 100 W air-plasma and exhibits a 180 mV higher overpotential towards OER at 0.5 mA/cm^2 than the same electrode previously reduced electrochemically. Thus, Pt substrates are particularly convenient to study OER electocatalysts. Finally, glassy carbon is another common substrate for in situ experiments. It is a non-graphitizing allotrope of carbon[48] that can be fabricated in thin films by controlled pyrolysis of photoresist materials.[49] Its wide inert potential range and stability[36,50] renders it indispensable in the studies of electrocatalysts.[51] Even as thin films, no features are observable besides hydrogen and oxygen evolution, both occurring at high overpotentials as shown in Fig. 6b for acidic and alkaline electrolytes. Furthermore, it also provides minimal electron scattering and low background contrast, often making it the substrate of choice for ec-LPTEM. It is however significantly more fragile, requiring care in handling and deposition of catalysts, and suffers from poor adhesion to the substrate and passivation layers. In summary, the choice of a material as working electrode substrate entails trade-offs, and we strongly recommend to carefully test the suitability of electrode substrates prior to performing the electrocatalytic processes of interest.

Reference electrode.—Choice of the RE is equally important to the success of an ec-LPTEM experiment and knowledge of the reference potential is essential for accurate interpretation of the electrochemical results. A number of studies have been dedicated to detailing the fundamental and practical aspects of REs,[52,53] including a recent review by Alnoush *et al*. focusing on their use in the context of microscale systems for in situ and *operando* studies of electrocatalysts.[54] Herein, we outline a few general guidelines and recommendations to keep in mind regarding this component of the liquid cell. The main requirements for REs are that its potential should be stable over time and ideally known (calibrated) for a given system and that their presence in the system should not contaminate the electrolyte.[54–56] Fundamentally, this implies that the electrolytic process determining the electrode potential should be well-defined, simple, and fast (has a high exchange current density), and should obey the Nernst equation.[55–57] Furthermore, the species partaking in the process (e.g., ionic species in solution and metallic electrode) should remain at equilibrium without altering the thermodynamic activities. This has led to conventional REs working in saturated conditions, separated from the external test solution by a liquid junction.[56] These systems are necessarily complex, and despite efforts to scale down electrodes such as the Ag/AgCl reference to sizes amenable to microsystems,[53,55] integration within chips for ec-LPTEM remains yet out of reach. Instead, ec-LPTEM systems conventionally feature a quasireference electrode in the form of a noble metal thin film, typically gold or platinum. The main difference of these electrodes is their direct contact with the environment of the cell, so that their potential does not result from a single, well-defined redox couple but instead from a combination of all electrolytic processes occurring in the vicinity of the electrode, resulting in a situation of mixed potential.[52–54] In practice, these electrodes can be particularly stable if there can be enough time to reach equilibrium and a stable liquid environment is provided. However, because their potential cannot be determined from the Nernst equation, they require calibration before and/or after each experiment, with radical changes expected based on the actual composition of the electrolyte and the state of the electrode surface. Furthermore, the small scale and proximity of all electrodes in the ec-LPTEM systems warrant caution regarding the stable environment assumption. For example, it is expected that the $H^+_{(aq)}/H_{2(g)}$ and $PtO_{(s)}/Pt_{(s)}$ redox couples contribute to the potential of a Pt quasireference electrode, which implies a relationship to the partial hydrogen pressure and pH.[54,58,59] This bears implication for the shape and distance of the electrodes in experiments where electrocatalytic processes at the working or counter electrodes can result in local pH changes or hydrogen evolution. The reference should therefore be placed sufficiently far away from the other electrodes, ideally upflow if possible. At the same time, the reference electrode should be close enough to the WE to minimize the uncompensated resistance R_u that depends on the conductivity of the solution and the distance between RE and WE. In the MEMS chip configuration where all electrodes are patterned on the same chip, the RE is relatively close to the WE with the distance being around several hundred micrometers. The values of R_u in such configuration, measured by electrochemical impedance spectroscopy (EIS), are around several tenths to several hundred ohms in aqueous electrolytes (unpublished measurements). With the current (i) in the range of several hundred nA in the microcell, the ohmic drop (iR_u) then falls in the range of several hundred μV and can usually be considered negligible. Apart from the stability of the redox couples on the Pt quasireference electrode, the possible exposure of the Ti or Cr adhesion layer underneath the Pt quasireference electrode can also influence the stability of the reference potential.[53]

Next, we describe the methodology to calibrate the reference potential value of the quasireference Pt thin-film electrodes typically used for the liquid-cell experiments. A reasonable approach is to measure its potential against an external bulk reference electrode such as the Ag/AgCl RE in the same electrolyte that is used for the electrochemical reactions. Another method to calibrate the Pt quasireference electrode is to add a redox pair with known redox potential in the electrolyte as an internal reference. For example, the equilibrium potential of ferricyanide/ferrocyanide ($[Fe(CN)_6]^{3-}/[Fe(CN)_6]^{4-}$) redox

pair is known to be at ~0.4 V vs standard hydrogen electrode (SHE).[60] Thus, the ferrocyanide/ferricyanide redox couple can be added in the electrolyte so the potential of the quasireference electrode can be calibrated from the known potential of the redox couple. It is worth noting that for electrocatalysis, the applied potential normally refers to the RHE. This is considered as a subtype of the SHE which is based on the hydrogen redox half reaction ($2H^{+}_{(aq)} + 2e^{-} \leftrightarrow H_{2(g)}$, 0 V vs SHE at pH 0). To convert the applied potential refering to RHE, the pH of the electrolyte needs to be considered within the Nernst equation:

$$E(V\ vs\ RHE) = E(V\ vs\ SHE) + 0.059 \times pH.$$

Finally, we note that previous studies have demonstrated with success the implementation of an external true reference, typically placed in a container outside of the specimen holder and connected to the microcell via the fluidic lines.[61–63] This configuration does however add significant ohmic resistance and noise due to the length and small cross-section of the fluidic lines, and we have typically found its implementation impractical for this reason. The next-generation in situ TEM holders that feature a dedicated cavity in close vicinity of the tip to host a miniaturized bulk RE are promising in that regard. Figure 7a shows a schematic of the new generation ec-LPTEM holders with an external bulk Ag/AgCl reference electrode that is incorporated on the tip (Hummingbird Scientific). We further demonstrate the calibration of Pt quasireference electrode using the on-the-tip Ag/AgCl RE. The potential difference between the Pt thin-film quasireference electrode and external Ag/AgCl RE in pH 13 KOH electrolyte is ~ -0.06 V. Since the standard electrode potential of an Ag/AgCl bulk RE versus SHE is $E_{Ag/AgCl} = 0.2$ V vs. SHE, the applied potential that is referred to RHE using Pt quasireference electrode in the pH 13 KOH electrolyte can be converted to:

$$E(V\ vs\ RHE) = E(V\ vs\ Pt) + 0.2 - 0.06 + 0.059 \times 13.$$

Figure 7b shows the CV curves of Co_3O_4 particles that were dropcast on a Pt working electrode using the different reference electrodes. The red curves depict three CV cycles acquired using an external bulk Ag/AgCl RE that is incorporated on the tip of the new generation ec-LPTEM holders (Hummingbird Scientific, Fig. 7b). The blue curves show the CV cycles of the same working electrode in the same cell using the calibrated Pt quasireference electrode. In both CV measurements, the pre-peak feature of Co_3O_4 at 1.5 V vs. RHE in the liquid cell in 0.1 M KOH electrolyte represents the redox Co III/IV and is in good agreement with the value reported in the literature using bulk electrochemical cells in 0.1 M KOH solution.[64]

Counter electrode.—The counter electrode of the electrochemical chips used in ec-LPTEM experiments is also important and, like the other electrodes, the scale of the apparatus bears implications for the choice of material and geometry, which should be considered with attention. The counter electrode provides(or sinks) the charges required for a reaction to happen at the working electrode. Therefore, its size should be properly tailored to ensure that processes at the WE are not limited by poor reaction or diffusion rates at the CE.[51] Furthermore, because its potential is not controlled but it is established as a result of the working electrode being driven by the potentiostat, care should be given that no parasitic reactions interfere with the observations and results. For instance, an easily oxidized CE may suffer from anodic dissolution when cycling catalysts at cathodic potential relevant to HER or CO_2RR at the WE. This, in turn, can result in reduction and redeposition of the dissolved ions on the catalyst thereby altering the observation.[65] In conventional benchtop cells, this problem is easily solved by using an ion conductive membrane, separating the cell in two chambers, and preventing contamination,[51] but this thus far remains out of reach for ec-LPTEM setups. Another issue can arise from gas evolution, typically happening when high anodic potentials are applied at the WE for instance to study OER catalysts. In this case, a small platinum CE would quickly reach potentials negative enough to induce HER, possibly disrupting the observations or modifying the quasireference electrode potential. For these reasons, it is good practice to monitor the potential of the CE versus the reference during experiments. Two strategies can be employed to avoid these effects. First, an electrochemically inert material (e.g., glassy carbon) can be used that evolves gas instead of partaking in dissolution/oxidation, while ensuring that the surface area ratio of CE to WE is large enough, and the current densities at the CE are therefore low enough to avoid gas nucleation. Second, an electrode with a relatively high capacitance (e.g. carbon black, platinum with large area) can be used with a carefully controlled surface area ratio, so that all charges required for reactions to happen at the WE can be provided or stored by the counter electrode's double layer capacitance. There again, holders accommodating for small cavities allowing to place an external CE in the vicinity of the tip but outside of the microcell are promising.

Electrocatalytic Applications

In this section, we discuss the electron imaging/probing and electrochemical considerations in relation to specific electrocatalytic processes. We begin with the most cathodic reaction, the CO_2 electroreduction, and establish conditions for performing ec-LPTEM that are relevant to electrocatalytic evolution of metallic nanoparticles. We continue with establishing control experiments for monitoring the ageing of metallic oxygen reducing catalysts and we close by demonstrating the breadth of information that can be acquired using ec-LPTEM by illustrating the analytic capabilities of probing the reaction product of oxygen-evolving oxide catalysts.

CO_2RR.—CO_2RR has the potential of converting waste CO_2 into value added chemicals such as CO, methane, ethylene, or ethanol through many electron and proton transfer steps.[66,67] The reaction is typically carried out in aqueous (neutral or alkaline) environment where the CO_2 is either dissolved in the electrolyte or supplied to the catalyst as a gas on a triple phase boundary at reducing potentials typically between -0.3 and -1.4 V vs RHE.[66] The selectivity and activity of this conversion rely primarily on a suitable catalyst.[68] Multiple catalyst classes exist. Homogeneous or supported molecular catalysts are limited to simple reaction products, CO or formate. Carbon matrix anchored single atom catalysts also typically produce CO or formate, but can achieve conversions to higher reduction products by fine tuning the active site.[69] Metallic catalysts, mostly in the form of nanoparticles, such as Bi, Sn, Ag, Au, and Zn, are all active for CO or formate production.[70–74] Notably Cu and Cu-based catalysts can produce a plethora of higher reduction products, such as methane, ethylene, or propanol.[67,75] Hydrogen evolution reaction has lower reduction potential and is often competing with CO_2RR.[76]

To study these catalysts in ec-LPTEM, given the considerations described above, a suitable supporting WE should have minimal activity for CO_2RR and the competing HER, which rules out the typical Pt or Au electrodes. Carbon as a supporting electrode material is ideal, it has no activity for CO_2RR and a large overpotential for HER.[27] Among the allotropes of carbon, the non-graphitizing glassy carbon is often used in the H-cell design to screen catalyst activity for CO_2RR.[77,78] Integration of glassy carbon microelectrodes is possible and provides a support with low resistivity and low background activity while having very little contrast, thus not interfering with imaging of nanocatalysts.[11] CO_2RR products are mostly gases and they nucleate as gas bubbles once the liquid electrolyte is fully saturated with gaseous products. These bubbles might disturb the catalyst observation as well as block off large portions of the working electrode in the confined electrolyte layer of ec-LPTEM microcells. For short experiments, the electrolyte can be kept stationary. With careful control over the applied currents/potentials, observations can be made before the bubbles start nucleating. For longer experiments, the electrolyte can be

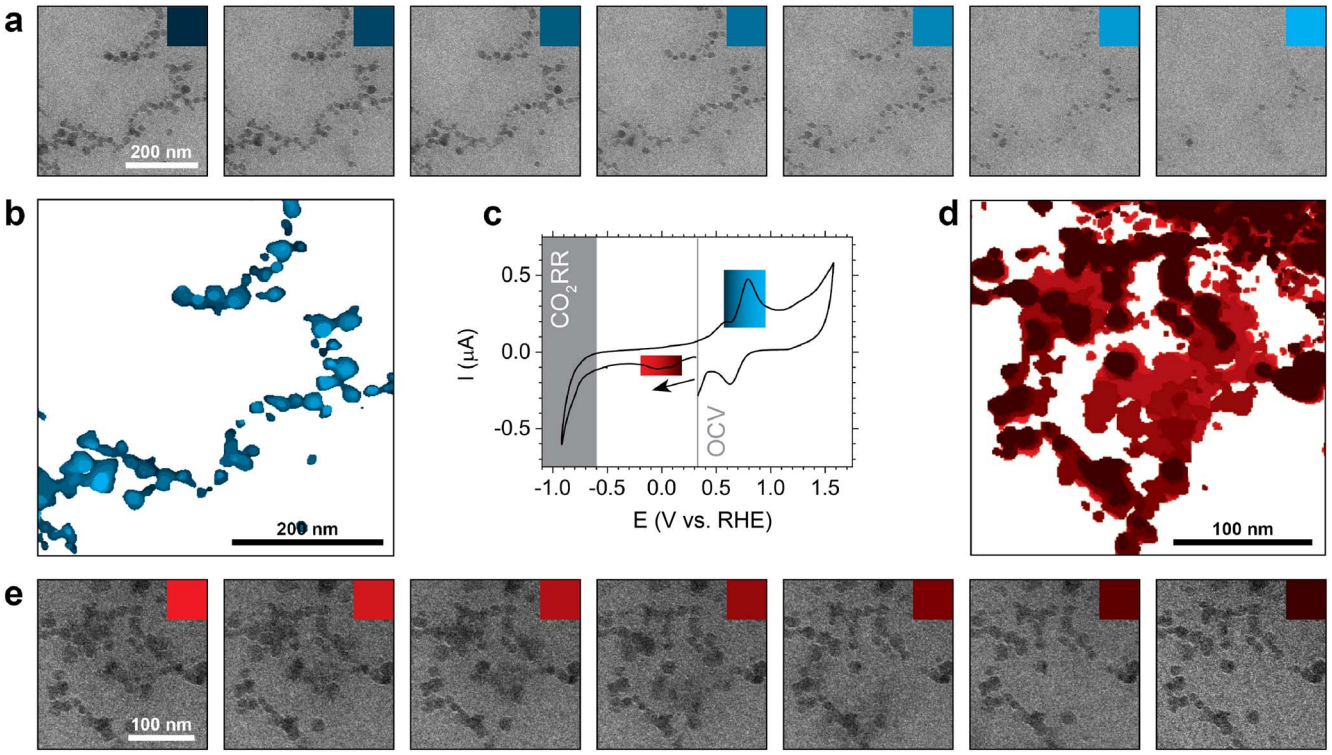

Figure 8. Morphology of redeposited Cu catalyst for CO_2RR during cyclic voltammetry loaded on a glassy carbon WE, in a cell with Pt CE and RE electrodes. (a) BFTEM image series documenting a dissolution event during an oxidation wave in the voltammogram. (b) Segmented particle projection visualizing the dissolution event. Color code corresponds to the particle projection from the images above. (c) CV scan starting from OCV at 0.3 V vs. RHE, first sweeping through the cathodic feature causing particle redeposition (red gradient), then reaching potentials relevant for CO_2RR around −1 V vs. RHE. The CO_2RR range is indicated on the basis of values in Ref. 80. Oxidative potentials are reached on the return scan, causing catalyst dissolution (blue gradient). (d) Segmented particle projection of the deposition event. Color code corresponds to the BFTEM images (e). Dose rate was 30 $e^{-}nm^{-2}s^{-1}$.

pumped through the imaging area to supply the catalyst with CO_2 and remove reaction products. Loading of the catalyst should be confined to the WE. For typical Cu catalysts it is especially important to avoid loading of the catalyst on the CE, as the Cu will oxidatively dissolve from the CE and likely redeposit on the WE, which might disturb the process under study.[79]

Next, we demostrate ec-LPTEM for CO_2RR on Cu nanocatalysts using cyclic voltammetry. The in-house fabricated glassy carbon electrode was initially loaded with a compact layer of 7 nm Cu spheres. The Cu nanoparticles were loaded to the WE by dropcasting the suspension from a glass micropipette mounted to a mechanical micromanipulator under an optical microscope. The microcell was filled with static 0.1 M $KHCO_3$ electrolyte saturated with CO_2. The activated/redeposited catalyst was observed in a BFTEM mode and zero-loss energy filtering (slit width 10 eV) was implemented to remove the inelastically scattered electrons and improve contrast. An electron dose rate of 30 $e^{-}nm^{-2}s^{-1}$ was used where no morphology changes were detected due to the observation itself. A relatively large initial field of view of 1.2 × 1.2 μm was sampled at 2048 × 2048 pixels at 20 frames per second using a direct electron camera (DirectElectron). This large (seemingly oversampled) dataset enabled in finding a suitable balance between spatial and temporal resolution during the data analysis.

Figures 8a & 8e depict the BFTEM images of dissolution and deposition processes of activated Cu nanocatalysts. The experiment began at open circuit voltage (OCV) around 0.35 V vs. RHE where the catalyst spontaneously undergoes slow dissolution.[11] The potential was first swept in the cathodic direction to more negative values. A reduction feature around 0 V vs. RHE is apparent in the voltammogram in Fig. 8c. This potential corresponds to reduction of Cu_2O and Cu^{+} to metallic Cu. Cu^{+} ions initially dissolved at OCV and deposition of multiple Cu particles was observed and highlighted with the red gradient in Figs. 8d & 8e. The cathodic scan continued until −1 V vs. RHE, where this catalyst would typically be operated. No morphological changes were observed during this short excursion to CO_2RR, apart from some particle movement. On the return anodic scan, a twin oxidation feature is apparent in the voltammogram after passing the OCV. The major peak at 0.8 V vs. RHE corresponds to the Cu^{0} to Cu^{2+} transition and it is highlighted with a blue gradient. At these potentials the Cu catalyst oxidatively dissolves from the WE, as demonstrated in Figs. 8a & 8b. On the return scan to OCV, there are additional reduction features, but no catalyst redeposition was observed in the field of view.

Overall, our findings suggest that careful monitoring of the electrochemical variables is essential towards obtaining relevant measurements on Cu catalysts, as both the reduction and oxidation potentials are close to OCV. Furthermore, the crystalline structure can be monitored in situ with the use of SAED to discern between metallic Cu, Cu_2O and CuO.[11] Similar considerations related to optimization of the imaging conditions and electrochemical protocols are also valid for CO_2RR catalysts other than Cu.

ORR.—The oxygen reduction is an important reaction pertaining to a variety of electrochemical systems for energy conversion, including proton exchange membrane fuel cells (PEMFC), alkaline fuel cells, solid oxide fuel cells (SOFC), and Li-air batteries.[81,82] The four electron pathway ($O_2 + 4H^{+} + 4e^{-} \rightarrow 2H_2O$ in aqueous acid medium) suffers however from sluggish kinetics at low temperature and requires significant amount of catalysts for improved reaction rates.[83] Pt and its alloys (with Co, Ni, and Fe, for example) remain the most used catalysts to date due to their high specific activity, but their stability during operation hinders the broad rollout of technologies relying on them.[84] Ec-LPTEM offers a significant opportunity for studying the degradation pathways of these catalysts in real-time and under realistic conditions.[9] This technique has been utilized to study commercial and state-of-the-art materials, most often in

conditions relevant to PEMFCs,[85] revealing mechanisms of metal dissolution, dealloying, coalescence and ripening, while also providing insights into corrosion of the catalyst support material.[12,21,61,86]

General considerations for the study of ORR catalysts in ec-LPTEM involve the choice of liquid electrolyte and electrochemical conditions. Relevant to PEMFC, electrocatalysts are cycled in aqueous acid medium (H_2SO_4 or $HClO_4$) in a potential range typically from < 0.6 to > 1.0 V vs. RHE, mimicking extreme scenarios found in the startup or shutdown of the devices inspired by the accelerated stress tests (AST) commonly performed in rotating disk electrode (RDE) or fuel cell stack setups.[87] Degradation is induced by the repeated cycling above potentials of Pt dissolution ($Pt \rightarrow Pt^{2+} + 2e^-$) and/or of PtO formation and subsequent chemical dissolution ($Pt + H_2O \rightarrow PtO + 2H^+ + 2e^-$ then $PtO + 2H^+ \leftrightarrow Pt^{2+} + H_2O$), both significant above 0.8 V vs. RHE. Carbon support corrosion (typically above 1.1 V vs. RHE) also plays a role in the device performance.[88] Consequently, the chosen substrate should be stable in this potential range and chemical environment, and ideally inert to OER.

To demonstrate the evolution of ORR catalysts for PEMFC applications, we performed a degradation experiment on 12 nm Pt nanocubes. The catalyst was dropcast on a chip fabricated in-house, featuring a glassy carbon WE, and two Pt electrodes as reference and counter. Imaging was performed in BFTEM mode, with zero-loss energy filtering and in thin-film wetting conditions to maximize resolution. Prior to the experiment, stable imaging conditions were determined, with an upper electron dose rate limit set at 120 e^- nm^{-2} s^{-1} where no e-beam induced damage could be observed to the sample. Electrochemical stimulus was applied by cyclic voltammetry at 500 mV s^{-1}, with a potential range set to 0.4 and 1.45 V vs. RHE for 360 cycles. Under these conditions, the timescale of degradation was expected to be on the order of tens of minutes. Therefore, the framerate was chosen to be 1 image per minute (every ~14 cycles) in order to limit the electron irradiation while maintaining adequate temporal resolution to track changes.

Figures 9a–9g show a time series of images from an aggregate of Pt nanocubes under CV cycling. Modification of the catalyst was observed over time, with particles becoming increasingly rounded and aggregating. Segmentation of each frame allowed to construct the projection map shown in Fig. 9h, which further demonstrates the morphological changes of the catalyst during the consecutive cycles of Pt oxidation and reduction (Fig. 9i). From the segmented images, quantification of the relative projected area loss as a function of cycle was performed on 5 different aggregates and is plotted in Fig. 9h. Significant loss in the catalyst projected area was observed after ~240 cycles. Two control measurements were also performed to verify the absence of e-beam induced degradation. First, an area was exposed to the electron beam under illumination conditions similar to the degradation experiment, but without biasing. As shown in Fig. 9j (green line), no apparent evolution of its morphology was observed within the 10 min of control experiment. Second, catalysts outside of the electron illuminated area were imaged before and after the degradation experiment and were found to have experienced similar degradation to the particles in the time-series, as shown from their relative area loss in Fig. 9j (black datum).

With these experiments, we conclude that the observed evolution of the Pt nanocubes results from cycling the catalyst under potential

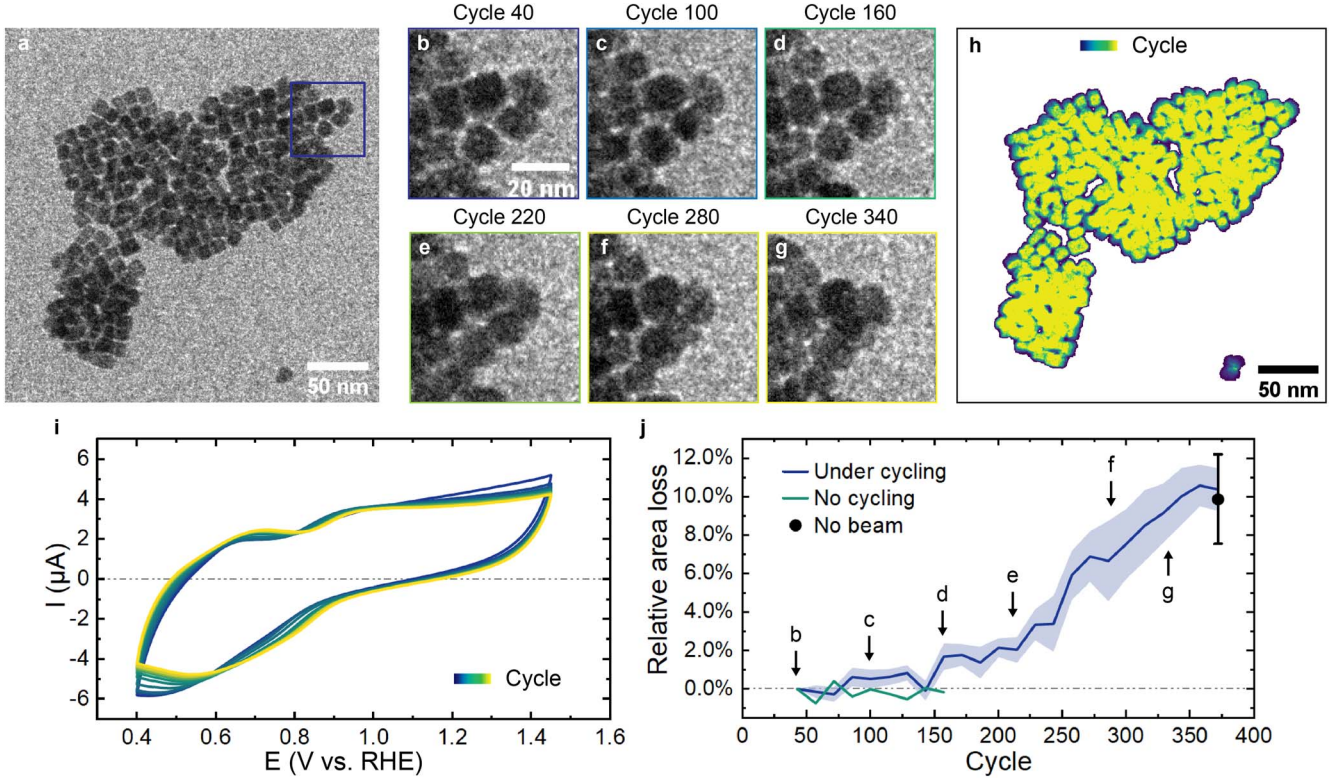

Figure 9. Dissolution and aggregation during accelerated stress test of Pt nanocubes catalysts for ORR. (a) BFTEM overview of an aggregate loaded on an electrochemical microchip fabricated in-house and featuring a glassy carbon WE, Pt CE and Pt RE. (b-g) time series of a close-up from (a) during cyclic voltammetry in the [0.4, 1.45] V vs RHE range at 500 mV s^{-1} in 0.1 M $HClO_4$. The potential was measured against the internal Pt reference during acquisition and corrected to RHE with E (V vs RHE) = E (V vs. Pt) + 0.8 V as measured from Pt HUPD features. Representative voltammograms throughout the cycling procedure are shown in (i). (h) Segmented particle projection visualizing the dissolution and aggregation event and the resulting area loss. Segmentation was performed in ImageJ with global thresholding using Otsu's method to set the threshold. (j) Relative projected area loss of Pt NCs aggregates plotted as a function of cycling advancement. Blue line and shaded area are the mean and one standard deviation over five aggregates. Green line (single measurement) and black point (mean, error bars are one standard deviation, N = 5) are control measurements performed in absence of bias or of e-beam illumination, respectively. In the absence of bias, the time series was converted to equivalent cycles for comparison. The area loss was calculated from the segmented images using the first frame as the reference and projected area measurements. Dose rate was 120 $e^-nm^{-2}s^{-1}$.

inducing platinum dissolution. This kind of experiment can therefore provide valuable information into the degradation pathways and kinetics of catalysts for ORR and their shape dependency.

OER.—Hydrogen gas, a renewable energy source stored in chemical bonds, is typically produced by water electrolysis. However, this technology is hindered by low efficiency, which is mostly due to the sluggish kinetics of the oxygen evolution reaction occurring at the anode. In alkaline solutions, hydroxide ions in the electrolyte dissociate and form molecular oxygen ($4OH^- \rightarrow 2O_2 + 2H_2O + 4e^-$). The four-electron pathway of the sluggish OER requires electrocatalysts to reduce the kinetic barrier of the reaction. To date, precious metal oxide catalysts, such as ruthenium and iridium oxides, are among the best oxide catalysts for OER showing both exceptional activity and stability.[89,90] RuO_2 shows better OER activity while IrO_2 is more stable in both alkaline and acidic media.[89,91] Recently, ec-LPTEM showed the capability to investigate OER oxide catalysts in real-time to understand the role of dynamic morphological evolution and its relationship to OER activity.[13] EELS in ec-LPTEM was reported to probe the product, molecular oxygen, in real-time, offering insights into understanding the activity and surface properties of Co-based oxide catalysts at single particle-level.[14]

To expand the operando chemical capabilities in ec-LPTEM for direct probing of electrocatalytic processes in alkaline medium in two dimensions, we use a benchmarked OER catalyst, IrO_2 nanoparticles. The particles were dropcasted on a customized thin-film Pt WE optimized for EELS acquisition in a liquid-cell enclosure with 0.1 M KOH electrolyte. Pt CE and RE were used. The electrodes were wetted with a thin liquid layer and the system was electrochemically operated with a constant anodic potential of 1.95 V vs. RHE . The EEL spectra were acquired using Gatan GIF Quantum ERS in a Thermal Fisher Scientific TEM at 300 kV. The collection angle was 19.8 mrad and the probe current was 0.2 nA. Spectrum Imaging was acquired with pixel dwell time = 1 s. Dual range EELS was applied to acquire both low-loss and core-loss EEL spectra.

Figure 10b shows the current response of chronoamperometry with the stabilization of the current occurring at ∼80 nA as time elapsed. The oxygen K-edge EEL spectra of two different positions are shown in Fig. 10c. The dark green spectrum that is acquired from the position closer to the IrO_2 particle shows a notable molecular oxygen feature at 531 eV. The bright contrast in the annular dark field (ADF) image (Fig. 10d) indicates the IrO_2 particle. Further, we calculated the relative thickness (in units of t/λ) where the center of the particle showed a relative thickness value as large as 2.5 while the t/λ was calculated to be ∼1.3 at the position close to the edge to the particle. The value of t/λ decreased to ∼1 further away from the particle. As the relative thickness reflects the overall thickness of the cell that is parallel to the electron-beam direction, its decreasing value with respect to the distance of the particle surface in-plane indicates a gradient of the liquid layer surrounding the particle.

For determining the molecular oxygen distribution around the IrO_2 particle under OER, the O K-edge EEL spectra at each pixel were fitted by three standard O K-edge EEL spectra: IrO_2, O_2, and liquid electrolyte. The multiple linear least-squares (MLLS) fitting coefficient of each component was performed in GMS software (Gatan) and it is qualitatively proportional to the amount of the component. The corresponding fitting coefficient maps of three components at O K-edge: IrO_2, molecular oxygen, and liquid electrolyte are shown in Fig. 10d. Prior to the fitting, the spectra were denoised by principal component analysis (PCA). The fitting coefficient map of IrO_2 does not match the ADF image of IrO_2. This may be due to the thickness of the IrO_2 particle, which could cause failure of the MLLS fitting process. The fitting coefficient map of O_2 shows that the value is higher at the position closer to the IrO_2 particle, qualitatively indicating the O_2 evolution from a single IrO_2 particle. The fitting coefficient map of the liquid electrolyte indicates that more liquid exists closer to the edge of the particle. The map is thus consistent with the relative thickness map.

Overall, the ability to acquire real-time chemical information and monitor the product formation at solid-liquid interfaces using EELS, is of exceptional relevance for many electrocatalytic processes. Herein, we showed that MLLS fitting can separate the contribution of different components in O K-edge EEL spectra, providing qualitatively O_2 and liquid electrolyte maps for oxygen-evolving oxide catalysts in two dimensions and thus directly relate the product with the surfaces that evolve it.

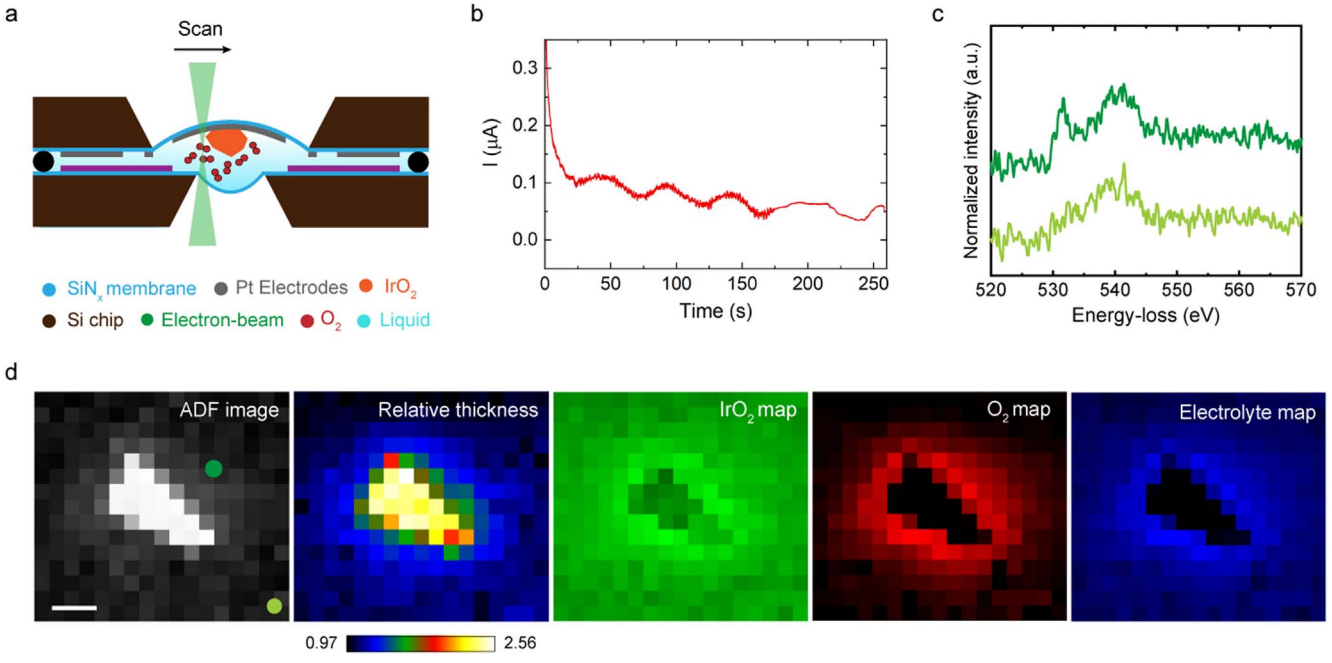

Figure 10. Chemical probing of molecular oxygen evolution near a single IrO_2 particle using STEM-EELS. (a) Schematic illustration of the microcell configuration. (b) Current response with respect to time of chronoamperometry at 1.95 V vs RHE. (c) Oxygen K-edge EEL spectra from two different regions. The dark green is closer to the particle while the light green is further. The positions at which the spectra were acquired are indicated as dark and light green spots in the ADF image. (d) ADF image and the corresponding maps of relative thickness, IrO_2, O_2, and electrolyte near the IrO_2 particle. Scale bar is 100 nm.

Conclusions

The capabilities of the ec-LPTEM at providing real-time morphological, structural, and even chemical information at high spatial and temporal resolution make it unique among characterization techniques. However, despite the advancements of ec-LPTEM for heterogeneous electrocatalysis that have been made since its first demonstration, it remains far from a routine technique since each experiment requires careful design and specific considerations have to be taken into account. Some of the current limitations could possibly be resolved with improvements in the design of the microcells, but the susceptibility of the system to the electron-beam induced effects will remain to be considered.

Within this methodological report, we showed that a critical parameter in the experiment is the overall cell thickness, influencing the contrast and spatial resolution of the studied electrocatalytic systems. To reduce the thickness of the liquid cell, the use of two-dimensional materials to seal the liquid in TEM has been demonstrated and atomically-resolved TEM images have been reported using graphene liquid cells.[92,93] However, these architectures are currently not compatible with electrochemical experiments due to lack of electrodes. The co-planar electrode configuration with thin liquid layer in the TEM electrochemical cell is associated with diffusion gradients that differ from the bulk geometries, often resulting in specific electrochemical characteristics. To understand the observed phenomena, it is helpful to simulate the electrochemical behavior and extract information such as region-specific current densities and potential distributions. These simulations, preferably computed in three-dimensions,[94] are also well-suited to guide the design of TEM electrochemical cells. Further developments should be focused on advancing the microfabrication of the electrochemical liquid cell to improve the quality of the acquired TEM data while maintaining relevant conditions for the specific electrocatalytic process under investigation. Particular interest lies in the observations of triple phase boundaries as often the reactants or products of the investigated heterogeneous electrocatalysis are in gaseous phase.

The electron-beam induced effects are a critical concern in ec-LPTEM. There can be no design of the liquid cell that can circumvent the interaction of the incident electron beam with the electrolytes or the catalysts. Such interactions potentially result in alteration of the properties and concentration of the species in the electrolytes as we discussed. Furthermore, radiolysis products due to the electron beam may interact with the studied materials, leading to unwanted reactions or degradation of the catalysts. This effect can be minimized as much as possible by carefully selecting the imaging conditions and using the minimal necessary electron dose. Some of the low-dose strategies such as electron counting detectors or compressed sensing may prove to be useful to reduce the effects.[14] The minimal necessary electron dose rate typically depends on the configuration of the liquid cell and varies with the combination of electrolyte and materials that compose the catalytic system under investigation. We recommend performing control experiments under the same acquisition conditions without electrochemical stimulus, such as demonstrated and discussed herein, to provide an understanding of the electron-beam induced effects. This can be particularly useful to determine the minimal necessary dose rate for the ec-LPTEM experiments. Finally, scavenger additives in the electrolytes may as well mitigate unwanted radiolysis processes but the alteration of the electrolyte components may have an impact on the electrochemical reactions.[19,20]

With advances in instrumentation, ec-LPTEM is becoming relevant for an increasing number of technologies and stands to provide unique insights into electrochemical processes in heterogeneous electrocatalysis as well as aid in development of novel catalysts. Thus, establishing its relevance with respect to a bulk cell operation for the numerous electrocatalytic processes is critical.

Acknowledgments

The work was partially supported by EPFL and partially by the Swiss National Research Foundation (SNF) under award nos. 200021_175711 and CRSII5_180335. The authors thank Dr Martina Lihter for discussions and help with excess ligands removal from the Pt catalysts.

ORCID

Robin Girod https://orcid.org/0000-0001-7861-7818
Vasiliki Tileli https://orcid.org/0000-0002-0520-6900

References

1. Y. Yang et al., *ACS Catal.*, **11**, 1136 (2021).
2. M. Wang and Z. Feng, *Chem. Commun.*, **57**, 10453 (2021).
3. M. Choi et al., *Nano Lett.*, **20**, 1233 (2020).
4. J. T. Mefford et al., *Nature*, **593**, 67 (2021).
5. M. R. Nellist et al., *Nat. Energy*, **3**, 46 (2018).
6. M. Risch et al., *Energy Environ. Sci.*, **8**, 661 (2015).
7. L. Trotochaud, A. R. Head, O. Karslıoğlu, L. Kyhl, and H. Bluhm, *J. Phys. Condens. Matter*, **29**, 053002 (2017).
8. M. Favaro et al., *JACS*, **139**, 8960 (2017).
9. N. Hodnik, G. Dehm, and K. J. J. Mayrhofer, *Acc. Chem. Res.*, **49**, 2015 (2016).
10. Y. Li et al., *Proceedings of the National Academy of Sciences*, **117**, 9194 (2020).
11. J. Vavra, T.-H. Shen, D. Stoian, V. Tileli, and R. Buonsanti, *Angew. Chem.*, **133**, 1367 (2021).
12. A. Impagnatiello et al., *ACS Appl. Energy Mater.*, **3**, 2360 (2020).
13. N. Ortiz Peña et al., *ACS Nano*, **13**, 11372 (2019).
14. T.-H. Shen, L. Spillane, J. Peng, Y. Shao-Horn, and V. Tileli, *Nat. Catal.*, **5**, 30 (2022).
15. J. Lee, D. Nicholls, N. D. Browning, and B. L. Mehdi, *Phys. Chem. Chem. Phys.*, **23**, 17766 (2021).
16. N. de Jonge, L. Houben, R. E. Dunin-Borkowski, and F. M. Ross, *Nature Reviews Materials*, **4**, 61 (2019).
17. M. E. Holtz, Y. Yu, J. Gao, H. D. Abruña, and D. A. Muller, *Microsc. Microanal.*, **19**, 1027 (2013).
18. N. M. Schneider et al., *J. Phys. Chem. C*, **118**, 22373 (2014).
19. E. Sutter et al., *Nat. Commun.*, **5**, 4946 (2014).
20. J. Korpanty, L. R. Parent, and N. C. Gianneschi, *Nano Lett.*, **21**, 1141 (2021).
21. V. Beermann et al., *Energy Environ. Sci.*, **12**, 2476 (2019).
22. J. J. Vlassak and W. D. Nix, *J. Mater. Res.*, **7**, 3242 (1992).
23. D. B. Peckys, G. M. Veith, D. C. Joy, and N. De Jonge, *PLoS One*, **4**, 8214 (2009).
24. G. Zhu et al., *Chem. Commun.*, **49**, 10944 (2013).
25. R. Serra-Maia et al., *ACS Nano*, **15**, 10228 (2021).
26. M. E. Holtz et al., *Nano Lett.*, **14**, 1453 (2014).
27. R. Girod, N. Nianias, and V. Tileli, *Microsc. Microanal.*, **25**, 1304 (2019).
28. H. Wu et al., *Small Methods*, **5**, 2001287 (2021).
29. M. N. Yesibolati et al., *Nanoscale*, **12**, 20649 (2020).
30. M. J. Williamson, R. M. Tromp, P. M. Vereecken, R. Hull, and F. M. Ross, *Nat. Mater.*, **2**, 532 (2003).
31. Q. Tseng, *thesis, Université de Grenoble* (2011), (https://tel.archives-ouvertes.fr/tel-00622264).
32. P. Vennemann, (2021), https://github.com/eguvep/jpiv.
33. A. Van Blaaderen and A. Vrij, *Langmuir*, **8**, 2921 (1992).
34. B. Kirby, *Micro- and Nanoscale Fluid Mechanics* (Cambridge University Press, Cambridge) (2010).
35. S. Keskin, P. Kunnas, and N. De Jonge, *Nano Lett.*, **19**, 4608 (2019).
36. J. D. Benck, B. A. Pinaud, Y. Gorlin, and T. F. Jaramillo, *PLoS One*, **9**, 107942 (2014).
37. P. Malinský, P. Slepička, V. Hnatowicz, and V. Švorčík, *Nanoscale Res. Lett.*, **7**, 241 (2012).
38. G. J. Brug, M. Sluyters-Rehbach, J. H. Sluyters, and A. Hemelin, *J. Electroanal. Chem. Interfacial Electrochem.*, **181**, 245 (1984).
39. S. Henning, J. Herranz, and H. A. Gasteiger, *J. Electrochem. Soc.*, **162**, F178 (2014).
40. L. Jacobse, S. J. Raaijman, and M. T. M. Koper, *Phys. Chem. Chem. Phys.*, **18**, 28451 (2016).
41. P. Daubinger, J. Kieninger, T. Unmüssig, and G. A. Urban, *Phys. Chem. Chem. Phys.*, **16**, 8392 (2014).
42. S. Cherevko, A. R. Zeradjanin, G. P. Keeley, and K. J. J. Mayrhofer, *J. Electrochem. Soc.*, **161**, H822 (2014).
43. J. Greeley, T. F. Jaramillo, J. Bonde, I. Chorkendorff, and J. K. Nørskov, *Nat. Mater.*, **5**, 909 (2006).
44. J. K. Nørskov et al., *J. Electrochem. Soc.*, **152**, J23 (2005).
45. T. Reier, M. Oezaslan, and P. Strasser, *ACS Catal.*, **2**, 1765 (2012).
46. A. Damjanovic and B. Jovanovic, *J. Electrochem. Soc.*, **123**, 374 (1976).
47. V. I. Birss and A. Damjanovic, *J. Electrochem. Soc.*, **134**, 113 (1987).
48. W. E. Van der Linden and J. W. Dieker, *Anal. Chim. Acta*, **119**, 1 (1980).
49. Y. M. Hassan et al., *J. Anal. Appl. Pyrolysis*, **125**, 91 (2017).
50. H. E. Zittel and F. J. Miller, *Anal. Chem.*, **37**, 200 (1965).

51. C. Wei et al., *Adv. Mater.*, **1806296**, 1 (2019).
52. U. Guth, F. Gerlach, M. Decker, W. Oelßner, and W. Vonau, *J. Solid State Electrochem.*, **13**, 27 (2009).
53. G. Inzelt, A. Lewenstam, and F. Scholz, *Handbook of Reference Electrodes* (Berlin, Springer) Vol. 344, p. XII (2013).
54. W. Alnoush, R. Black, and D. Higgins, *Chem Catalysis*, **1**, 997 (2021).
55. M. W. Shinwari et al., *Sensors*, **10**, 1679 (2010).
56. D. T. Sawyer, A. Sobkowiak, J. L. Roberts, and D. T. Sawyer, *Electrochemistry for Chemists* (New York, Wiley) 2nd ed., p. 505 (1995).
57. G. Jerkiewicz, *ACS Catal.*, **10**, 8409 (2020).
58. J. Ghilane, P. Hapiot, and A. J. Bard, *Anal. Chem.*, **78**, 6868 (2006).
59. S. Park et al., *Anal. Chem.*, **77**, 7695 (2005).
60. J. E. O'Reilly, *Biochimica et Biophysica Acta (BBA) - Bioenergetics*, **292**, 509 (1973).
61. S. Nagashima et al., *Nano Lett.*, **19**, 7000 (2019).
62. J. Lim et al., *Science*, **353**, 566 (2016).
63. R. R. Unocic et al., *Microsc. Microanal.*, **20**, 1029 (2014).
64. A. Bergmann et al., *Nat. Catal.*, **1**, 711 (2018).
65. J. G. Chen, C. W. Jones, S. Linic, and V. R. Stamenkovic, *ACS Catal.*, **7**, 6392 (2017).
66. S. Nitopi et al., *Chem. Rev.*, **119**, 7610 (2019).
67. Y. Hori, K. Kikuchi, and S. Suzuki, *Chem. Lett.*, **14**, 1695 (1985).
68. D. Gao, R. M. Arán-Ais, H. S. Jeon, and B. Roldan Cuenya, *Nat. Catal.*, **2**, 198 (2019).
69. F. Franco, C. Rettenmaier, H. S. Jeon, and B. Roldan Cuenya, *Chem. Soc. Rev.*, **49**, 6884 (2020).
70. H. S. Jeon et al., *JACS*, **140**, 9383 (2018).
71. W. Zhu et al., *JACS*, **135**, 16833 (2013).
72. C. Kim et al., *JACS*, **137**, 13844 (2015).
73. S. Zhang, P. Kang, and T. J. Meyer, *JACS*, **136**, 1734 (2014).
74. Z. Zhang et al., *ACS Catal.*, **6**, 6255 (2016).
75. X. Zhang, S. X. Guo, K. A. Gandionco, A. M. Bond, and J. Zhang, *Materials Today Advances*, **7**, 100074 (2020).
76. A. Goyal, G. Marcandalli, V. A. Mints, and M. T. M. Koper, *JACS*, **142**, 4154 (2020).
77. R. Reske, H. Mistry, F. Behafarid, B. Roldan Cuenya, and P. Strasser, *JACS*, **136**, 6978 (2014).
78. A. Loiudice et al., *Angew. Chem.*, **128**, 5883 (2016).
79. F. D. Speck and S. Cherevko, *Electrochem. Commun.*, **115**, 106739 (2020).
80. D. Kim, C. S. Kley, Y. Li, and P. Yang, *PNAS*, **114**, 10560 (2017).
81. V. R. Stamenkovic, D. Strmcnik, P. P. Lopes, and N. M. Markovic, *Nature Mater*, **16**, 57 (2017).
82. R. M. Ormerod, *Chem. Soc. Rev.*, **32**, 17 (2003).
83. M. Shao, Q. Chang, J.-P. Dodelet, and R. Chenitz, *Chem. Rev.*, **64**, 3594 (2016).
84. J. Fan et al., *Nat. Energy*, **6**, 475 (2021).
85. A. P. Soleymani, L. R. Parent, and J. Jankovic, *Adv. Funct. Mater.*, **33**, 2209733 (2021).
86. G. Z. Zhu et al., *J. Phys. Chem. C*, **118**, 22111 (2014).
87. S. Martens et al., *J. Power Sources*, **392**, 274 (2018).
88. D. J. Myers, X. Wang, M. C. Smith, and K. L. More, *J. Electrochem. Soc.*, **165**, F3178 (2018).
89. Y. Lee, J. Suntivich, K. J. May, E. E. Perry, and Y. Shao-Horn, *J. Phys. Chem. Lett.*, **3**, 399 (2012).
90. K. A. Stoerzinger et al., *Chem*, **2**, 668 (2017).
91. N. Danilovic et al., *J. Phys. Chem. Lett.*, **5**, 2474 (2014).
92. J. M. Yuk et al., *Science*, **336**, 61 (2012).
93. D. J. Kelly et al., *Adv. Mater.*, **33**, 2100668 (2021).
94. M. Binggeli, T.-H. Shen, and V. Tileli, *J. Electrochem. Soc.*, **168**, 106508 (2021).